This paper is published as part of a PCCP Themed Issue on:

Physical chemistry of solids – the science behind materials engineering

Guest Editors: Jürgen Janek, Manfred Martin and Klaus Dieter Becker

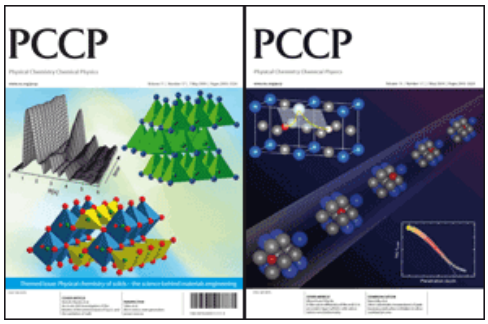

Editorial

Physical chemistry of solids—the science behind materials engineering
Phys. Chem. Chem. Phys., 2009
DOI: 10.1039/b905911n

Perspectives

Nanoionics: ionic charge carriers in small systems
Joachim Maier, *Phys. Chem. Chem. Phys.*, 2009
DOI: 10.1039/b902586n

Micro-ionics: next generation power sources
Harry L. Tuller, Scott J. Litzelman and WooChul Jung, *Phys. Chem. Chem. Phys.*, 2009
DOI: 10.1039/b901906e

Communications

On the conduction pathway for protons in nanocrystalline yttria-stabilized zirconia
Sangtae Kim, Hugo J. Avila-Paredes, Shizhong Wang, Chien-Ting Chen, Roger A. De Souza, Manfred Martin and Zuhair A. Munir, *Phys. Chem. Chem. Phys.*, 2009
DOI: 10.1039/b901623f

Direct calorimetric measurement of grain boundary and surface enthalpies in yttria-stabilized zirconia
Shushu Chen, Hugo J. Avila-Paredes, Sangtae Kim, Jinfeng Zhao, Zuhair A. Munir and Alexandra Navrotsky, *Phys. Chem. Chem. Phys.*, 2009
DOI: 10.1039/b819740g

Papers

Elastic strain at interfaces and its influence on ionic conductivity in nanoscaled solid electrolyte thin films—theoretical considerations and experimental studies
N. Schichtel, C. Korte, D. Hesse and J. Janek, *Phys. Chem. Chem. Phys.*, 2009
DOI: 10.1039/b900148d

Chemical and electronic properties of the ITO/Al_2O_3 interface
Yvonne Gassenbauer, André Wachau and Andreas Klein, *Phys. Chem. Chem. Phys.*, 2009
DOI: 10.1039/b822848e

Electronic state of oxygen nonstoichiometric $La_{2-x}Sr_xNiO_{4+\delta}$ at high temperatures
Takashi Nakamura, Keiji Yashiro, Kazuhisa Sato and Junichiro Mizusaki, *Phys. Chem. Chem. Phys.*, 2009
DOI: 10.1039/b823364k

B-Site cation diffusivity of Mn and Cr in perovskite-type $LaMnO_3$ with cation-deficit nonstoichiometry
Shogo Miyoshi and Manfred Martin, *Phys. Chem. Chem. Phys.*, 2009
DOI: 10.1039/b901208g

High anion conductivity in a ternary non-equilibrium phase of BaF_2 and CaF_2 with mixed cations
B. Ruprecht, M. Wilkening, A. Feldhoff, S. Steuernagel and P. Heitjans, *Phys. Chem. Chem. Phys.*, 2009
DOI: 10.1039/b901293a

Electrical and optical characterization of undoped $BaTiO_3$ in the quenched state
K.-D. Becker, M. Schrader, H.-S. Kwon and H.-I. Yoo, *Phys. Chem. Chem. Phys.*, 2009
DOI: 10.1039/b823174e

Oxidation states of Co and Fe in $Ba_{1-x}Sr_xCo_{1-y}Fe_yO_{3-\delta}$ (x, y = 0.2–0.8) and oxygen desorption in the temperature range 300–1273 K
Ashley S. Harvey, F. Jochen Litterst, Zhen Yang, Jennifer L. M. Rupp, Anna Infortuna and Ludwig J. Gauckler, *Phys. Chem. Chem. Phys.*, 2009
DOI: 10.1039/b819414a

Bulk defect chemistry and surface electronic behavior of Zn,Sn codoped In_2O_3 transparent conducting oxides
Steven P. Harvey, Thomas O. Mason, Christoph Körber and Andreas Klein, *Phys. Chem. Chem. Phys.*, 2009
DOI: 10.1039/b822149a

Defect chemistry of the cage compound, $Ca_{12}Al_{14}O_{33-\delta}$—understanding the route from a solid electrolyte to a semiconductor and electride
Doh-Kwon Lee, Lutz Kogel, Stefan G. Ebbinghaus, Ilia Valov, Hans-Dieter Wiemhoefer, Martin Lerch and Juergen Janek, *Phys. Chem. Chem. Phys.*, 2009
DOI: 10.1039/b818474g

Electrical conductivity–defect structure correlation of variable-valence and fixed-valence acceptor-doped $BaTiO_3$ in quenched state
Han-Ill Yoo, Tae-Sik Oh, Hyung-Soon Kwon, Dong-Kyu Shin and Jong-Sook Lee, *Phys. Chem. Chem. Phys.*, 2009
DOI: 10.1039/b822381p

An *in situ* XAS investigation of the kinetics of the ammonolysis of Ga_2O_3 and the oxidation of GaN
J. Brendt, D. Samuelis, T. E. Weirich and M. Martin, *Phys. Chem. Chem. Phys.*, 2009
DOI: 10.1039/b901819k

***In situ* investigation of coloration processes in $LiNbO_3$: MgO during reducing/oxidizing high-temperature treatments**
Dmytro Sugak, Yaroslav Zhydachevskii, Yuriy Sugak, Oleg Buryy, Sergii Ubizskii, Ivan Solskii, Alexander Börger and Klaus-Dieter Becker, *Phys. Chem. Chem. Phys.*, 2009
DOI: 10.1039/b822631h

Voltage-assisted ^{18}O tracer incorporation into oxides for obtaining shallow diffusion profiles and for measuring ionic transference numbers: basic considerations
J. Fleig, *Phys. Chem. Chem. Phys.*, 2009
DOI: 10.1039/b822415c

Oxygen incorporation into strontium titanate single crystals from CO_2 dissociation
Chr. Argirusis, F. Voigts, P. Datta, J. Grosse-Brauckmann and W. Maus-Friedrichs, *Phys. Chem. Chem. Phys.*, 2009
DOI: 10.1039/b901401b

Nearly constant loss effects in borate glasses
David M. Laughman, Radha D. Banhatti and Klaus Funke, *Phys. Chem. Chem. Phys.*, 2009
DOI: 10.1039/b822561n**Switching behaviour of modulated ferroelectrics I: kinetics of the field-induced lock-in transition of Rb_2ZnCl_4**
K. Elisbihani, H. Gibhardt and G. Eckold, *Phys. Chem. Chem. Phys.*, 2009
DOI: 10.1039/b902368b

Construction of nano- and microporous frameworks from octahedral bubble clusters
S. M. Woodley, M. B. Watkins, A. A. Sokol, S. A. Shevlin and C. R. A. Catlow, *Phys. Chem. Chem. Phys.*, 2009
DOI: 10.1039/b902600b

Bubbles and microporous frameworks of silicon carbide
M. B. Watkins, S. A. Shevlin, A. A. Sokol, B. Slater, C. R. A. Catlow and S. M. Woodley, *Phys. Chem. Chem. Phys.*, 2009
DOI: 10.1039/b902603g

Band gap engineering of ZnO *via* doping with manganese: effect of Mn clustering
Hilkka Saal, Thomas Bredow and Michael Binnewies, *Phys. Chem. Chem. Phys.*, 2009
DOI: 10.1039/b901596e

Transport pathways for mobile ions in disordered solids from the analysis of energy-scaled bond-valence mismatch landscapes
Stefan Adams and R. Prasada Rao, *Phys. Chem. Chem. Phys.*, 2009
DOI: 10.1039/b901753d

Ultrathin oxide films and heterojunctions: CaO layers on BaO and SrO
Chris E. Mohn, Neil L. Allan and John H. Harding, *Phys. Chem. Chem. Phys.*, 2009
DOI: 10.1039/b822588e

Formation entropies of intrinsic point defects in cubic In_2O_3 from first-principles density functional theory calculations
Péter Ágoston and Karsten Albe, *Phys. Chem. Chem. Phys.*, 2009
DOI: 10.1039/b900280d

Hydrogen adsorption on Pd-containing Au(111) bimetallic surfaces
Sudha Venkatachalam and Timo Jacob, *Phys. Chem. Chem. Phys.*, 2009
DOI: 10.1039/b900250b

Interdiffusion and surface-sandwich ordering in initial Ni-core–Pd-shell nanoparticle
Alexander V. Evteev, Elena V. Levchenko, Irina V. Belova and Graeme E. Murch, *Phys. Chem. Chem. Phys.*, 2009
DOI: 10.1039/b822112j

First-principles study on defect chemistry and migration of oxide ions in ceria doped with rare-earth cations
Masanobu Nakayama and Manfred Martin, *Phys. Chem. Chem. Phys.*, 2009
DOI: 10.1039/b900162j**An electrochemical study of lithium insertion into $Cr_{5-y}Ti_ySe_8$ (y = 1, 2, 3, 4, 4.5) beyond the intercalation limit**
Sylvio Indris, Joseph Wontcheu and Wolfgang Bensch, *Phys. Chem. Chem. Phys.*, 2009
DOI: 10.1039/b822397a

Mixed $LiCo_{0.6}M_{0.4}PO_4$ (M = Mn, Fe, Ni) phosphates: cycling mechanism and thermal stability
Natalia N. Bramnik, Dmytro M. Trots, Heiko J. Hofmann and Helmut Ehrenberg, *Phys. Chem. Chem. Phys.*, 2009
DOI: 10.1039/b901319a

Changes in the crystal and electronic structure of $LiCoO_2$ and $LiNiO_2$ upon Li intercalation and de-intercalation
Sonja Laubach, Stefan Laubach, Peter C. Schmidt, David Ensling, Stefan Schmid, Wolfram Jaegermann, Andreas Thißen, Kristian Nikolowski and Helmut Ehrenberg, *Phys. Chem. Chem. Phys.*, 2009
DOI: 10.1039/b901200a

Partial oxidation of methanol on well-ordered V_2O_5(001)/Au(111) thin films
J. M. Sturm, D. Göbke, H. Kuhlenbeck, J. Döbler, U. Reinhardt, M. V. Ganduglia-Pirovano, J. Sauer and H.-J. Freund, *Phys. Chem. Chem. Phys.*, 2009
DOI: 10.1039/b822384j

Investigation of the nucleation and growth dynamics of FePt nanoparticles prepared *via* a high-temperature synthesis route employing $PtCl_2$ as platinum precursor
Hauke Heller, Kirsten Ahrenstorf, Jose A. C. Broekaert and Horst Weller, *Phys. Chem. Chem. Phys.*, 2009
DOI: 10.1039/b822306h

Non-oxidic nanoscale composites: single-crystalline titanium carbide nanocubes in hierarchical porous carbon monoliths
Kirstin Sonnenburg, Bernd M. Smarsly and Torsten Brezesinski, *Phys. Chem. Chem. Phys.*, 2009
DOI: 10.1039/b822437d

Poly(p-phenylene sulfone)s with high ion exchange capacity: ionomers with unique microstructural and transport features
C. C. de Araujo, K. D. Kreuer, M. Schuster, G. Portale, H. Mendil-Jakani, G. Gebel and J. Maier, *Phys. Chem. Chem. Phys.*, 2009
DOI: 10.1039/b822069g

Pulsed electrodeposition of porous ZnO on Ag-coated polyamide filaments
Melanie Rudolph, Thomas Loewenstein, Elisa Arndt, Yvonne Zimmermann, Andreas Neudeck and Derck Schlettwein, *Phys. Chem. Chem. Phys.*, 2009
DOI: 10.1039/b822534f

Oxidation states of Co and Fe in $Ba_{1-x}Sr_xCo_{1-y}Fe_yO_{3-\delta}$ (x, y = 0.2–0.8) and oxygen desorption in the temperature range 300–1273 K

Ashley S. Harvey,*[a] F. Jochen Litterst,[b] Zhen Yang,[a] Jennifer L. M. Rupp,[a] Anna Infortuna[a] and Ludwig J. Gauckler[a]

Received 3rd November 2008, Accepted 14th January 2009
First published as an Advance Article on the web 11th February 2009
DOI: 10.1039/b819414a

Four compositions of $Ba_{1-x}Sr_xCo_{1-y}Fe_yO_{3-\delta}$ were studied for phase, oxygen uptake–release, and transition metal (TM) oxidation states after solid state processing and with *in situ* heating from 300 to 1273 K in air. X-Ray diffraction showed that all compositions except one had the cubic perovskite structure at all temperatures; that with x, y = 0.2 was a mixture as prepared, becoming predominantly cubic at high temperature. Thermogravimetry showed a reversible oxygen absorption–desorption of approximately ±1% from 700 to 1273 K. X-Ray absorption and Mössbauer spectroscopy showed a majority TM^{3+} valence, with at most 40% TM^{4+}. Up to a temperature of 1073 K, the TM^{4+} was reduced to TM^{3+}. Further heating of the composition with x, y = 0.2 to 1233 K resulted in the reduction of Co^{3+} to Co^{2+}. Results from room temperature measurements confirm the thermally activated carrier hopping mechanism with charge fluctuations, while the high temperature delocalized carrier conductivity occurs with a small amount of TM reduction and without phase change for the initially cubic samples.

Introduction

In the search for solid oxide fuel cell (SOFC) cathodes to operate at intermediate temperatures (*e.g.* 673–973 K), perovskites (ABO_3) are often targeted for tailoring of their transport characteristics through materials engineering. This can be accomplished by A- or B-site substitution as well as oxygen stoichiometry control. In 2004, $Ba_{0.5}Sr_{0.5}Co_{0.8}Fe_{0.2}O_{3-\delta}$ was found to give a higher SOFC power output than the current standard $La_{0.4}Sr_{0.6}Co_{0.2}Fe_{0.8}O_{3-\delta}$.[1] Since then, compositions of $Ba_{1-x}Sr_xCo_{1-y}Fe_yO_{3-\delta}$ (BSCF) have been more heavily investigated with varying values of x and y for their structural, electronic, and ionic properties. Compared to similar materials at intermediate temperatures, BSCF has the advantage of being a mixed ionic–electronic conductor with high ionic conductivity and acceptable electronic conductivity.[2–4] Some authors have shown that compositions of BSCF can remain in a stable cubic perovskite structure with unusually high oxygen deficiency (values of δ) and over a broad temperature range,[5,6] while a recent publication demonstrates the formation of a hexagonal phase from the meta-stable cubic perovskite over time at temperatures less than 1073 K;[7] both findings have implications on the structural stability of BSCF. Other researchers have begun to address the usability of BSCF in intermediate temperature applications where CO_2 is present because its adsorption and the subsequent formation of carbonate material under such conditions adversely affect SOFC performance.[8]

In SOFCs, the cathode is typically exposed to air and temperatures of 673–973 K or higher. For BSCF, the oxidation states of Co and Fe and the oxygen non-stoichiometry affect the transport of electrons and ions through the material. If BSCF is to be engineered for and ultimately applied to SOFCs, we must first understand both its initial state and how it behaves under representative SOFC conditions. A few studies have already been undertaken to examine BSCF with methods that include *in situ* heating and, as mentioned above, different gas environments. X-Ray diffraction with heating to 1273 K in air and 1173 K in two low pO_2 gas environments was utilized by Wang *et al.* to study $Ba_{0.5}Sr_{0.5}Co_{0.8}Fe_{0.2}O_{3-\delta}$ membranes, and the perovskite structure was found under all conditions with reversible thermal expansion.[9] McIntosh *et al.* measured X-ray and neutron diffraction patterns of $Ba_{0.5}Sr_{0.5}Co_{0.8}Fe_{0.2}O_{3-\delta}$ with heating to 1273 K in various O_2 partial pressures and observed that the cubic phase was stable over all of their test conditions, and that the $3-\delta$ oxygen non-stoichiometry values ranged from about 2.15 to 2.35.[6] Finally, in the work of Ovenstone *et al.*, X-ray diffraction patterns of $Ba_{0.5}Sr_{0.5}Co_{1-y}Fe_yO_{3-\delta}$ (y = 0–1) with heating to 1273 K in low oxygen partial pressure environments showed that all samples were structurally stable to 1273 K with $pO_2 \geq 1 \times 10^{-5}$ bar, except y = 0, which underwent an irreversible transformation from hexagonal to cubic symmetry at about 1073 K. In a reducing gas mixture of H_2–N_2 (4% H_2) the decomposition temperature of the BSCF increased with increasing Fe content, occurring at 673 K for y = 0 and 1048 K for y = 1. Here, too, the phase changes were

[a] *Nonmetallic Inorganic Materials, Department of Materials, ETH Zürich, Wolfgang-Pauli-Str. 10, Zürich, CH-8093, Switzerland. E-mail: ashley.harvey@mat.ethz.ch; Fax: +41 (0)44 632 1132; Tel: +41 (0)44 632 3634*
[b] *Institute of Condensed Matter Physics, TU Braunschweig, Mendelssohn-Str. 3, D-38106 Braunschweig, Germany*

irreversible, though it should be noted that the cooling rate was 15 K min^{-1}.[10]

The purpose of this publication is to present results on the state of BSCF under conditions similar to the operation of a SOFC, as well as lower temperatures (300–800 K) that might be utilized in micro-SOFCs.[11] We examine for the first time the X-ray absorption spectroscopy of BSCF over a temperature range of 300–1233 K to determine the oxidation states of Co and Fe with *in situ* heating in air. The structural stability of BSCF over these temperatures was monitored with high temperature X-ray diffraction in air, and the oxygen stoichiometry of BSCF was investigated with thermogravimetry in air. The initial room temperature oxidation state and coordination of the Fe cations were determined with Mössbauer spectroscopy.

Experimental

$Ba_{1-x}Sr_xCo_{1-y}Fe_yO_{3-\delta}$ (BSCF) powder samples were prepared through solid state reaction of Fe_2O_3 (99 + %), Co_2O_3 (99 + %), $SrCO_3$ (99.9 + %), and $BaCO_3$ (99 + %). The detailed process is described elsewhere.[12] For this study, four compositions were chosen for analysis with $x = 0.5$, $y = 0.2$; $x = 0.5$, $y = 0.8$; $x = 0.2$, $y = 0.2$; and $x = 0.8$, $y = 0.2$. The mixed raw powders were planetary milled in a zirconia jar at a speed of 300 rpm for 30 min, and then passed through a 125 μm sieve to get finely ground raw powder. The green powders were then calcined in a platinum crucible at 1273 K for 6 h with a ramp rate of 3 K min^{-1} in a Nabertherm muffle furnace in air. Until their characterization with the following methods, the powders were stored in air in closed jars.

X-Ray absorption spectroscopy (XAS) and X-ray diffraction (XRD) measurements were taken on beamline BM01B (the Swiss–Norwegian Beam Lines) of the European Synchrotron Radiation Facility (ESRF, Grenoble, France). To measure the X-ray absorption, approximately 6 mg of each sample powder were ground and mixed with boron nitride powder and pressed into thin wafers. From the wafers, a slice of 1 mm × 10 mm was cut and placed in a quartz capillary tube with 1 mm diameter. The X-ray diffraction patterns were measured on powdered samples loosely packed in capillary tubes of 0.5 mm diameter. For both types of measurement the ends of the capillary tubes were snipped off so that the samples would be open to air, and synthetic air (O_2–N_2) was flowed through. During the XAS and XRD, the samples were heated *in situ* from 300 K to a maximum of 1233 K with an air blower positioned closely under the quartz tube sample holders. Heating and cooling rates were an average of 8 K min^{-1}. The intermediate and maximum measurement temperatures were based on regions defined by previous temperature-dependent conductivity measurements (Fig. 1, to be elaborated upon in a coming publication), and were selected to coincide with the regimes of localized and delocalized charge carriers. The XAS data were taken in transmission mode at the Co and Fe K edges (*ca.* 7709 and 7112 eV, respectively) and a Co or Fe metal foil was scanned simultaneously to obtain a reference for the calibration of the X-ray energy. The intrinsic energy resolution with use of the (111) cut Si monochromator was 1.4 eV, and the monochromator was detuned to 60% to reject

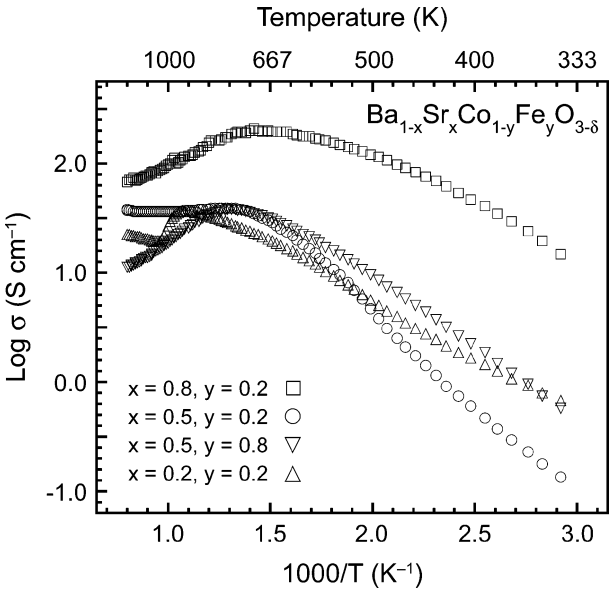

Fig. 1 Arrhenius plot of total conductivity *versus* temperature for all $Ba_{1-x}Sr_xCo_{1-y}Fe_yO_{3-\delta}$ samples showing the transitions from localized to delocalized charge carriers, the higher conductivity of composition $x = 0.8$, $y = 0.2$, and the higher transition temperature of composition $x = 0.2$, $y = 0.2$.

harmonics. A two-circle diffractometer equipped with six counting chains was employed for the XRD data acquisition, which allowed for pattern collection (2θ = 4–35°) in under 15 minutes. The energy of the X-rays was 24.83 keV, corresponding to a wavelength of 0.4994 Å.

The XAS data were processed using the program Athena, a component of the Ifeffit software suite.[13] The data were aligned to the metal foils, background-subtracted, and normalized to the area 75–175 eV above the edge onset, which was determined from the maximum in the first derivate of the spectrum. The cubic lattice parameters of the BSCF powders were calculated from several peaks between 10 and 30° 2θ of the XRD patterns.

Thermogravimetric (TG) measurements were measured on a Netzsch STA 449 C thermobalance/differential scanning calorimeter. About 640 mg of each sample were loaded into an alumina crucible and heated from 300 to 1273 K at a rate of 8 K min^{-1} in a synthetic air environment, and the heating program was cycled three times. The resulting weight loss was calibrated against that measured from an empty crucible under the same conditions.

^{57}Fe Mössbauer absorption experiments were performed in a standard transmission geometry using a ^{57}Co:Rh source with sinusoidal velocity sweep. The thickness of the powder absorbers corresponded to *ca.* 0.3 mg cm^{-2} ^{57}Fe. The hyperfine parameters were derived from least-squares fits of Lorentzian resonance lines to the spectral data. In the present paper we report only on the data collected at 300 K.

Results and discussion

In Fig. 2 the XRD patterns of $Ba_{0.2}Sr_{0.8}Co_{0.8}Fe_{0.2}O_{3-\delta}$ with *in situ* heating and cooling from 300 to 1073 K are shown.

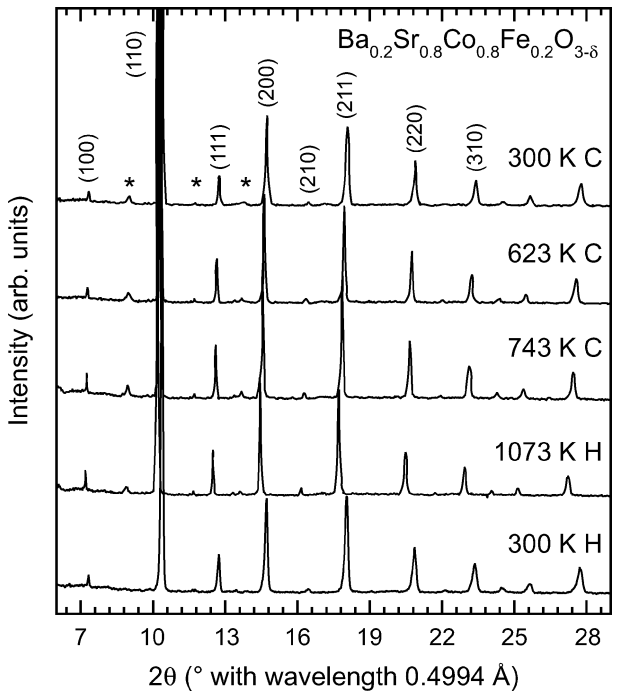

Fig. 2 XRD patterns of $Ba_{0.2}Sr_{0.8}Co_{0.8}Fe_{0.2}O_{3-\delta}$, where the cubic perovskite peaks are indexed and some small peaks from a secondary phase are marked with asterisks; H indicates heating, C cooling. Note that the vertical scale is set to display the lower intensity peaks, with the (110) peak cut off at the top.

These patterns are also representative of what is observed for samples with $x = 0.5$: $Ba_{0.5}Sr_{0.5}Co_{1-y}Fe_yO_{3-\delta}$. Before any heat is applied, the pure cubic perovskite phase ($Pm\bar{3}m$) is present, and the first eight reflections of this pattern are indexed in Fig. 2. Until the maximum temperature of 1073 K, no change is seen in the XRD except for the peaks moving to positions of smaller 2θ because of thermal expansion, so the diffraction patterns for the heating ramp are not shown. At 1073 K, three small peaks appear, marked with asterisks in Fig. 2. These peaks persist with cooling of the sample, and are most likely due to the formation of carbonates and/or simple oxides. Since only three peaks are observed and their intensities are very low, a definitive phase identification is difficult.

Table 1 shows the change in the cubic lattice parameter a (Å) with composition and temperature. Increasing amounts of Ba and Co enlarge the unit cell. The thermal expansion of all the BSCF compositions studied here is reversible, and the linear coefficients of thermal expansion calculated from the XRD data are also listed in Table 1. The calculation of these values was done by measuring the change in the (220) peak position with temperature and applying the formula $\alpha = \Delta L/(\Delta T \times L_0)$ where ΔL is the change in (220) plane spacing, ΔT is the change in temperature, and L_0 is the original (220) plane spacing at 300 K. No clear trend is present in the thermal expansion coefficients (TECs), but the values calculated here are in line with previous studies; note that the whole temperature range in our experiments was used for the calculation while others have claimed that the TECs of BSCF vary with temperature by as much as 10–15%.[4,5,10,14] From studies on $La_{0.8}Sr_{0.2}Co_{1-y}Fe_yO_3$ it seems that the TEC should increase with increasing Co content,[15] but our values and those of Zhu *et al.* are contrary to this.[16] Such a disagreement could be due to the rhombohedral crystal structure of the La-based perovskite *versus* the cubic BSCF or a difference in the mechanism of oxygen desorption between the material with a mixed charge at the A site (La^{3+}, Sr^{2+})(Co, Fe)$O_{3-\delta}$ and the constant A-site charge of (Ba^{2+}, Sr^{2+})(Co, Fe)$O_{3-\delta}$, where the general perovskite formula is ABO_3. Because the $x = 0.5$, $y = 0.8$ sample has a larger TEC than that of the $x = 0.5$, $y = 0.2$ sample, at 1073 K they have nearly the same lattice parameter, which indicates that the former composition loses oxygen more readily than the latter. The TEC minimum with respect to the Ba–Sr ratio at 50 : 50 has been shown already[3,16] and is consistent with findings for $La_{1-x}Sr_xCo_{0.2}Fe_{0.8}O_3$.[17]

Table 1 Cubic lattice parameters at room and maximum temperatures and linear coefficients of thermal expansion for all $Ba_{1-x}Sr_xCo_{1-y}Fe_yO_{3-\delta}$ samples based on XRD measurements from 300 to 1073 K for $x > 0.2$ and 300 to 1233 K for $x = 0.2$

x	y	a/Å (300 K)	a/Å (max. temp.)	α/K^{-1}
0.8	0.2	3.90	3.97	23.2×10^{-6}
0.5	0.2	3.98	4.03	16.5×10^{-6}
0.5	0.8	3.96	4.04	26.7×10^{-6}
0.2	0.2	4.03	4.10	17.3×10^{-6}

The XRD patterns of $Ba_{0.8}Sr_{0.2}Co_{0.8}Fe_{0.2}O_{3-\delta}$ with *in situ* heating from 300 to 1233 K and cooling are notably different from those of the other samples, as shown in Fig. 3. This composition shows at least two phases over all temperatures. The first eight peaks of the majority cubic phase, which is always present, are indexed in Fig. 3(a). In comparing the patterns at the starting room temperature and the maximum temperature of 1233 K, the minority phases change and the hexagonal phase that develops at 1233 K remains while the temperature is cooled back to 300 K. Fig. 3(b) shows the 2θ region around the most intense reflections of the primary cubic and secondary hexagonal phases and it is apparent that the fraction of the cubic phase increases with temperature. Other authors have reported only the presence of the cubic phase in high temperature XRD studies of BSCF, with the exception of the $x = 0.5$, $y = 0$ composition, which transformed from hexagonal to cubic at *ca.* 1073 K in 10^{-5} bar pO_2.[10] However, the range of these studies is limited to samples with $x = 0.5$.[6,9] The transformation to the cubic phase of $Ba_{0.8}Sr_{0.2}Co_{0.8}Fe_{0.2}O_{3-\delta}$ at higher temperature in air was confirmed by heating a sample to 1173 K for 30 h and air quenching to 300 K; the XRD pattern of this specimen (not shown) was purely cubic.

The TG results over the second heating and cooling cycle for $Ba_{0.5}Sr_{0.5}Co_{0.8}Fe_{0.2}O_{3-\delta}$ (representative of all compositions) are shown in Fig. 4 as percent mass *versus* temperature and are listed for all compositions in Table 2. The first heating of each sample creates the largest mass loss, particularly above 1000 K. Upon cooling the samples regain about 1% mass. The second thermal cycle—with *ca.* 1% mass loss and gain for heating and cooling, respectively—is in good agreement with previous reports showing a plateau with negligible mass loss from 300 to 700 K followed by a steady decrease in mass above 700 K.[2,10,16] The heating and cooling curves are nearly

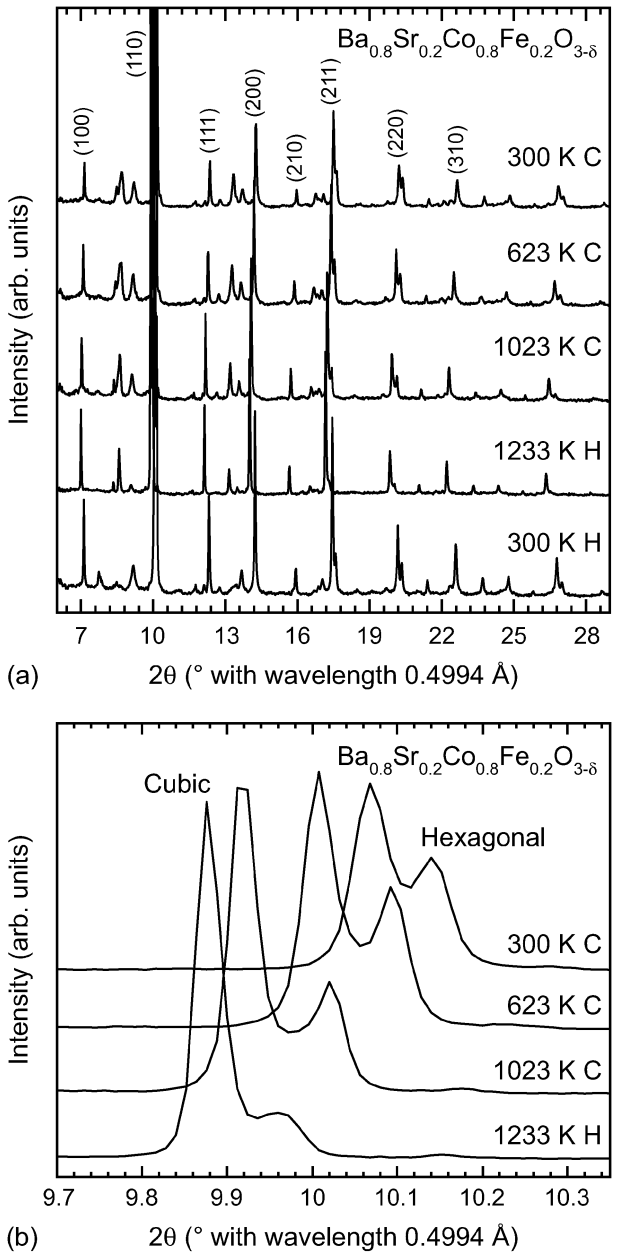

Fig. 3 (a) XRD patterns of $Ba_{0.8}Sr_{0.2}Co_{0.8}Fe_{0.2}O_{3-\delta}$, where the predominant cubic phase is indexed and the remaining peaks belong to a related hexagonal transformation; H indicates heating, C cooling. Note that the vertical scale is set to display the lower intensity peaks, with the (110) peak cut off at the top. (b) The strongest XRD peaks, showing the increase in the fraction of the hexagonal phase during cooling.

reversible, exhibiting the fast absorption and desorption of oxygen by BSCF.

The mass lost during heating in synthetic air from a totally pure sample is due to oxygen desorption with vacancy creation. Most of the loss of mass in the first heating cycle corresponds to the desorption of loosely bound, non-lattice oxygen species and contaminants such as hydroxyl or carbonate groups that may have condensed on the powdered samples that were stored in air or originated from starting materials that had not fully reacted. Note that this does not

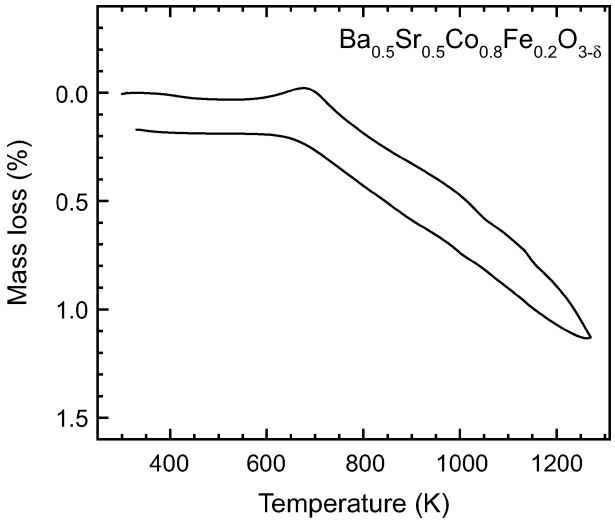

Fig. 4 TG of $Ba_{0.5}Sr_{0.5}Co_{0.8}Fe_{0.2}O_{3-\delta}$ (representative of all samples) with a rate of 8 K min^{-1}. The first heating cycle creates a significantly larger loss of mass due to the evaporation of volatile species, while further cycles show the reversible oxygen uptake and release.

Table 2 Percent mass lost during heating and regained during cooling over the second temperature cycle in synthetic air for all $Ba_{1-x}Sr_xCo_{1-y}Fe_yO_{3-\delta}$ samples

x	y	Heating	Cooling
0.8	0.2	−1.08%	+1.01%
0.5	0.2	−1.12%	+0.96%
0.5	0.8	−1.26%	+0.95%
0.2	0.2	−1.15%	+0.99%

affect the interpretation of the X-ray and conductivity data, as the former are not sensitive to surface effects and would respond proportionally to the percent mass of these "contaminants," and the latter were taken from samples heat treated prior to measurement. That the Fe-rich sample with $x = 0.5$ lost more mass than its Co-rich counterpart agrees with the XRD thermal expansion results described above and previous findings.[2,10] The mass loss that occurs above 700 K during the second cycle is the result of lattice oxygen desorption.

Mössbauer spectra were taken at room temperature for the $Ba_{1-x}Sr_xCo_{1-y}Fe_yO_{3-\delta}$ materials with $x = 0.5$, $y = 0.2$; $x = 0.5$, $y = 0.8$; $x = 0.2$, $y = 0.2$; and $x = 0.8$, $y = 0.2$ and additionally, for comparison, $x = 0.5$, $y = 1.0$. Fig. 5 shows a representative absorption spectrum with $x = 0.5$, $y = 0.8$ and its spectral decomposition with three quadrupole-split doublets.

The compositions $x = 0.5$, $y = 0.8$; $x = 0.8$, $y = 0.2$; and $x = 0.5$, $y = 1.0$ have very similar paramagnetic patterns consisting of three quadrupole doublets. Table 3 gives a summary of the hyperfine parameters obtained from fitting the Mössbauer data. Isomer shifts yield information on the oxidation state of iron and quadrupole splittings on the symmetries of electronic shells. The relative spectral areas reflect the relative populations of the various iron species. No attempt was made to correct for eventually different Debye–Waller factors for iron in different sites. From the

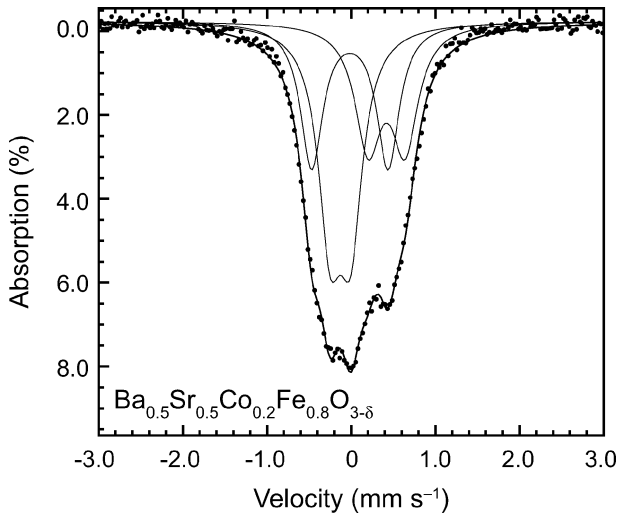

Fig. 5 ^{57}Fe Mössbauer absorption spectrum at 300 K of $Ba_{0.5}Sr_{0.5}Co_{0.2}Fe_{0.8}O_{3-\delta}$; the data are marked with dots, while the thin solid lines are the spectral decomposition with three quadrupole-split doublets.

isomer shifts, about 40% of the spectral weight can be attributed to Fe^{4+} in only slightly distorted octahedral oxygen coordination as concluded from the comparatively small quadrupole interaction. Two additional sites with similar spectral weights of about 25–30% each have charge states between Fe^{4+}–Fe^{3+} and Fe^{3+}–Fe^{2+}, respectively, as would be caused by rapid charge hopping between these states, so they are labeled with $Fe^{(3+\varepsilon)+}$ and $Fe^{(3-\varepsilon)+}$. The quadrupole interaction is relatively big and is also indicative of some valence contribution due to the non-integer oxidation state in a severely distorted surrounding, *e.g.* in the neighborhood of oxygen vacancies.

In contrast to these non-magnetic patterns, the compositions of $Ba_{1-x}Sr_xCo_{1-y}Fe_yO_{3-\delta}$ with $x = 0.2$, $y = 0.2$ and $x = 0.5$, $y = 0.2$ reveal magnetic hyperfine patterns already at room temperature. For $x = 0.2$, $y = 0.2$ we find a superposition of about 50% paramagnetic and 50% magnetically ordered fractions in agreement with the XRD, which reveals a phase mixture. The paramagnetic fraction is mostly $Fe^{(3+\varepsilon)+}$ (isomer shift 0.18 mm s^{-1}) with a smaller contribution by Fe^{5+} (isomer shift −0.43 mm s^{-1}, vanishing quadrupole splitting) typical for octahedral coordination. From the isomer shift (0.38 mm s^{-1}), the again nearly vanishing quadrupole interaction, and magnetic hyperfine field (45 T), the magnetic part can clearly be attributed to octahedral Fe^{3+}. The magnetic hyperfine field reveals some distribution, which can be connected to local distortions. For $x = 0.5$, $y = 0.2$ we also find a superposition of at least three magnetic patterns (fields between 42 and 46 T) from Fe^{3+}; however, additionally there is a broad unresolved background with a shift corresponding to Fe^{3+} with about 50% spectral weight. Whether this signal is due to a broad inhomogeneous distribution of magnetic moments or has a dynamical origin cannot be decided from these data.

Numerous Mössbauer studies on well-crystallized perovskite materials of a similar type have been reported in the literature.[18–20] Like our samples, various oxidation states of iron were found; however, they had highly symmetric surroundings as implied from vanishing electric field gradients, which is surprising in light of their five-fold oxygen coordinations.[18,20] But most of these studies were performed in the magnetically ordered regime where a distribution of electric field gradients with different sign and/or variable angles with respect to the magnetic hyperfine field may have resulted in an averaging of the quadrupole interaction. In the present samples, no signal that can be associated with an undistorted octahedral iron site is found. Quadrupole doublets with parameters close to doublets 1 and 3 (Table 3) have been reported for Ba-substituted $LaFeO_3$,[21] and were associated with Fe^{3+} and Fe^{4+} in an oxygen deficient neighborhood (note that the quadrupole splitting reported in ref. 21 is apparently defined as $\Delta = (1/4)e^2qQ$ whereas here the conventional $QS = (1/2)e^2qQ$ is used, with eq being the electric field gradient and Q the nuclear quadrupole moment). However, doublet 2 was not found.

Fig. 6 shows Fe (a) and Co (b) K edge spectra representative of the $Ba_{1-x}Sr_xCo_{1-y}Fe_yO_{3-\delta}$ powders. To show with the greatest clarity the X-ray absorption near edge structure (XANES) the compositions chosen for the figure are $x = 0.5$, $y = 0.8$ for iron and $x = 0.5$, $y = 0.2$ for cobalt. Since XAS is typically an averaging technique, the overall shapes of the spectra in Fig. 6 are much the same, but the details reveal important variations. Looking at the XANES, three main features are noted. (1) The pre-edge peak with maximum near 7114 eV (7710 eV) for Fe (Co). This is indicative of Fe (Co) 1s → 3d quadrupole transitions that are weakly allowed under imperfect octahedral symmetry and mixing of the metal 4p and 3d states, creating a dipole transition. (2) The K edge onset results from the transition metal (TM) 1s → 4p excitation, but can also be affected by local geometry around the absorbing ion and can be correlated to the metal oxidation state, with higher oxidation states resulting in higher energy onsets. (3) The most prominent peak just above the edge onset, sometimes called the white line, gives some information about the disorder or oxygen vacancies surrounding the absorber and also has been related to the metallic oxidation state. The structure at higher energies is mainly reflective of multiple scattering.[22]

Table 3 Hyperfine parameters of three iron sites in $Ba_{1-x}Sr_xCo_{1-y}Fe_yO_{3-\delta}$ with S1, 2, 3 isomer shifts against iron metal at 300 K; QS1, 2, 3 quadrupole splittings; and A1, 2, 3 relative spectral weights (error ± 2%). Numeral 1 corresponds to Fe^{4+}, 2 to $Fe^{(3+\varepsilon)+}$, and 3 to $Fe^{(3-\varepsilon)+}$. Results for samples with $x = 0.5$, $y = 0.2$ and $x = 0.2$, $y = 0.2$ are given in the text.

x	y	S1/mm s^{-1}	S2/mm s^{-1}	S3/mm s^{-1}	QS1/mm s^{-1}	QS2/mm s^{-1}	QS3/mm s^{-1}	A1 (%)	A2 (%)	A3 (%)
0.8	0.2	−0.015(5)	0.023(5)	0.421(5)	0.26(1)	0.85(1)	0.40(1)	44	26	30
0.5	0.8	−0.018(5)	0.094(5)	0.530(5)	0.24(1)	0.91(1)	0.43(1)	42	29	29
0.5	1.0	−0.031(5)	0.112(5)	0.585(5)	0.26(1)	0.98(1)	0.46(1)	51	26	23

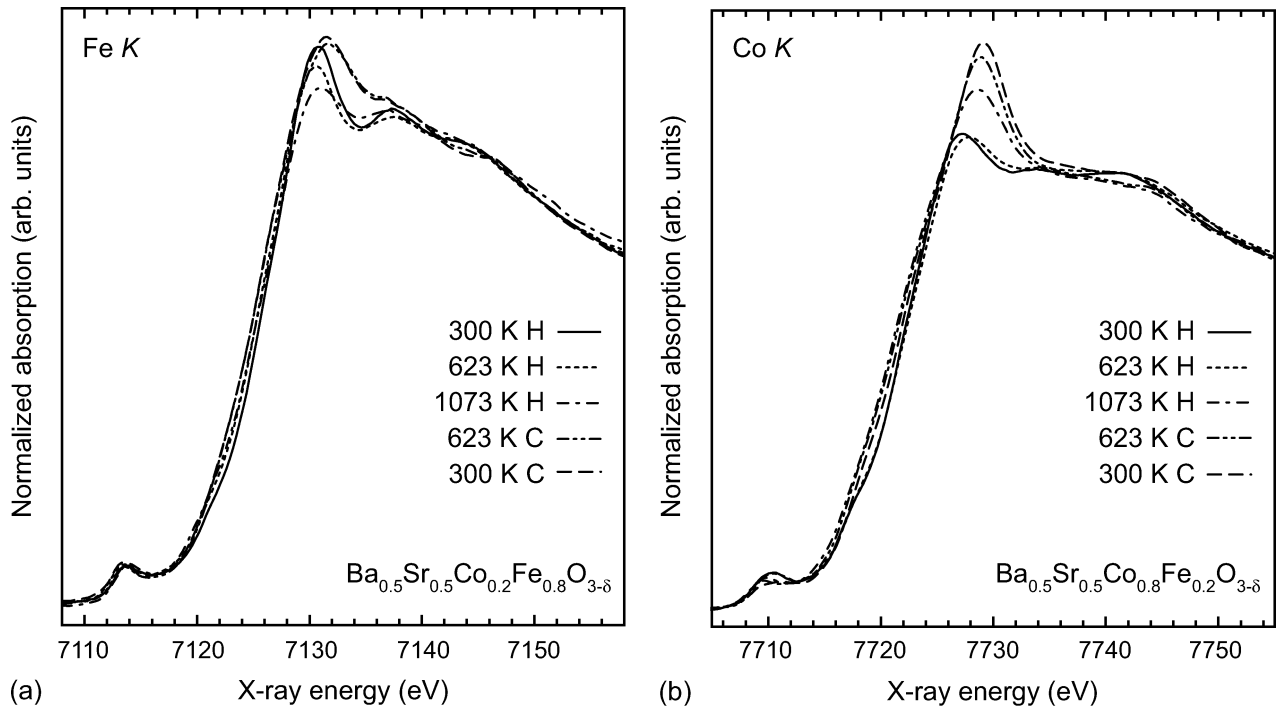

Fig. 6 Effect of changing temperature *in situ* on the XAS. (a) Fe K edge of $Ba_{0.5}Sr_{0.5}Co_{0.2}Fe_{0.8}O_{3-\delta}$. (b) Co K edge of $Ba_{0.5}Sr_{0.5}Co_{0.8}Fe_{0.2}O_{3-\delta}$. For both K edges, a gradual change occurs up to the localized–delocalized charge carrier transition range (*ca.* 775 K), after which a more dramatic change is observed, and the XANES is not fully recovered with cooling.

In the Fe K spectra in Fig. 6(a), which are characteristic of all the BSCF compositions studied here, starting at 300 K and increasing the temperature moves the edge onset about 1 eV lower; cooling the sample again to room temperature does not return the edge onset to its starting position. The intensity of the main Fe K peak decreases in relation to that of the additional higher energy peaks with heating and the overall edge shape appears flattened, as if the applied heat damps the oscillations of the XANES, and the structure is not recovered with cooling. The pre-edge peak changes little and is centered at about 7113.5 eV for all temperatures, putting the Fe average oxidation state near Fe^{3+} with some amount of Fe^{4+},[23] in agreement with the Mössbauer results. In the case of fully stoichiometric BSCF in the cubic perovskite structure, the point group of the TMO_6 (TM = Fe, Co) octahedra is centrosymmetric, and the pre-edge feature is due only to quadrupole interactions. However, with oxygen non-stoichiometry ($2.0 \leq (3-\delta) \leq 3.0$), which is certainly present, the symmetry around the TM cations will be non-centrosymmetric, resulting in an increase of the pre-edge peak intensity. (The imperfect octahedra are also found by Mössbauer spectroscopy.) In our experiment, the pre-edge peak intensity cannot be directly related to a change in TM oxidation state or coordination symmetry, since both occur simultaneously.

In the Co K spectra in Fig. 6(b), representative of all compositions except $x = 0.2$, $y = 0.2$, the edge onset shifts to lower energies with increasing temperature; however, the magnitude of the shift is dependent on the $Ba_{1-x}Sr_xCo_{1-y}Fe_yO_{3-\delta}$ composition. The edge shift ranges from about 1 eV for $x = 0.8$, $y = 0.2$ to almost 4 eV for $x = 0.2$, $y = 0.2$. A graphical summary of both the Fe and Co edge onset values with respect to temperature and composition is shown in Fig. 7, including the values for reference samples $LaFeO_3$ and $LaCoO_3$. The Co XANES shows an increase in the intensity of the main K edge peak relative to the higher energy structures as the temperature is raised to 1073 K and then lowered again to 300 K. The temperature-dependent Co K spectra for $Ba_{0.8}Sr_{0.2}Co_{0.8}Fe_{0.2}O_{3-\delta}$ are shown in Fig. 8. For this sample, the maximum temperature during measurement was 1233 K, 150 K higher than the other samples, because the transition of its electronic behavior from localized to delocalized charge carriers does not occur until almost 820 K and a return to localized behavior is observed above 1000 K (Fig. 1). The changes in the Co XANES for this sample are similar to the others but much more pronounced: more than a strong decrease in the edge onset energy and heightening of the main peak, a shoulder develops at about 7722 eV. Fig. 8(b) shows the pre-edge region of the spectra, where the Co 1s $\rightarrow$ 3d transitions take place, and the peak here loses intensity at higher temperature, which is a strong indication that the Co has been reduced. Furthermore, the pre-edge peak splitting increases, which could be the result of a larger crystal field splitting of the 3d level into its t_{2g} and e_g components.

Based on the Fe edge onsets [Fig. 7(a)], which for all the BSCF samples are slightly greater than that of $LaFeO_3$ at 300 K, the starting oxidation state is mostly Fe^{3+} but likely also includes some Fe^{4+}. With heat applied to transition from the localized (semiconductor) into the delocalized (metal-like) region of conductivity, the lower edge onset values indicate the reduction of Fe^{4+} to Fe^{3+}. Further reduction to Fe^{2+} is not observed and is not expected since this requires temperatures of *ca.* 1833 K.[24] At the Co edge [Fig. 7(b)], the onsets at

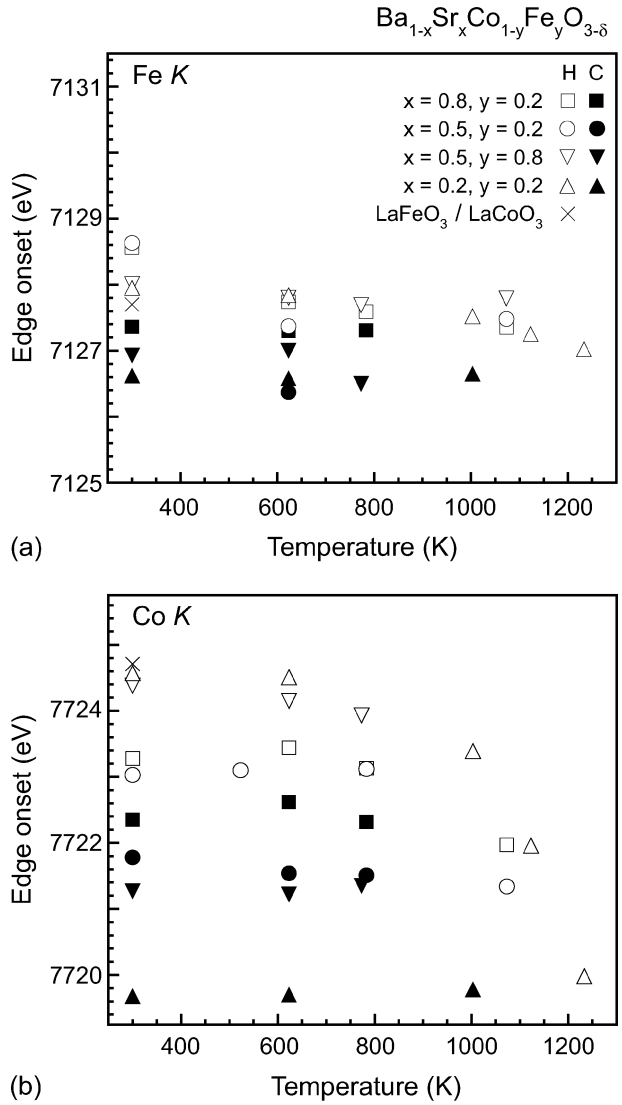

Fig. 7 Comparison of (a) Fe K edge onset and (b) Co K edge onset with changing temperature and composition. The legend in (a) applies to (b), and the scale of the ordinate is the same for both plots. The heating ramp is shown by open symbols, the cooling ramp by filled symbols. The error bars are similar to the sizes of the data icons.

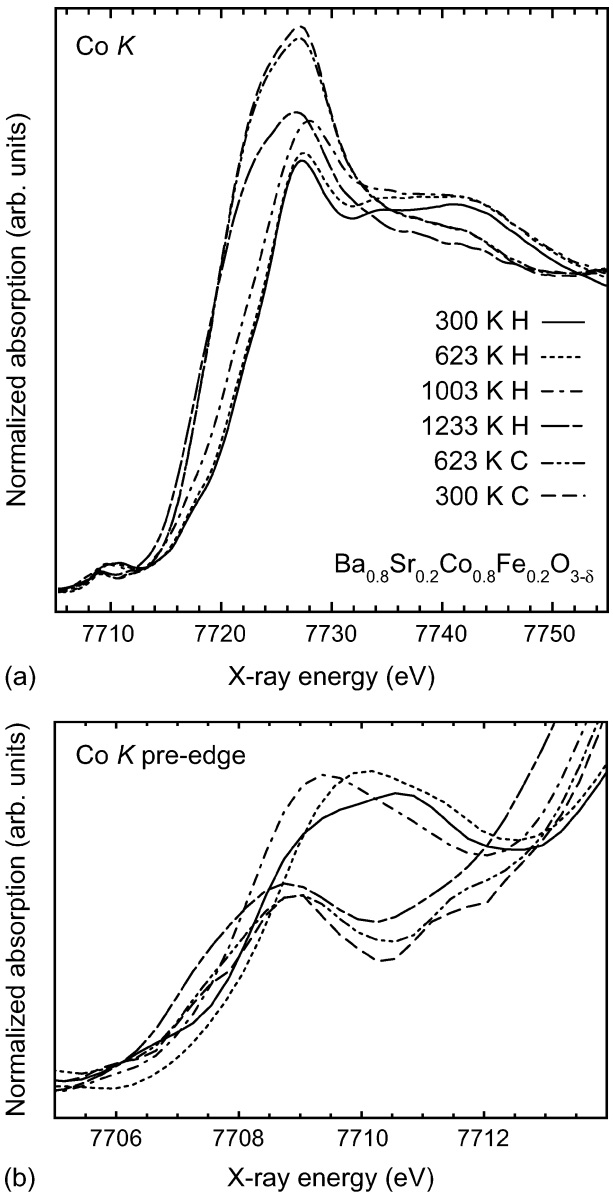

Fig. 8 Effect of changing temperature *in situ* on the XAS of $Ba_{0.8}Sr_{0.2}Co_{0.8}Fe_{0.2}O_{3-\delta}$. (a) Co K edge XANES. (b) Co K pre-edge.

300 K are nearly equal to ($x = 0.2$, $y = 0.2$; $x = 0.5$, $y = 0.8$) or a bit less than that of $LaCoO_3$ ($x = 0.5$, $y = 0.2$; $x = 0.8$, $y = 0.2$), indicating that the highest starting oxidation state is close to Co^{3+}. It is expected that more of the Fe is 4+ than Co since the former is more stable, but if the ^{57}Fe Mössbauer results are extended to the Co cations, a non-trivial amount of Co^{4+} is present. Increasing the temperature induces the reduction of any Co^{4+} to Co^{3+}. Only one of the four samples ($x = 0.2$, $y = 0.2$) was measured up to 1233 K, past the required 1173 K temperature for transformation from Co^{3+} to Co^{2+},[24] and this reduction is evident in the large edge shift and change in XANES for this sample.[25] Previous Fe and Co K edge XAS studies have shown that a negative edge shift of about 4 eV corresponds to the addition of one valence electron.[26]

It is interesting to note that at 300 K the BSCF composition with the lowest Fe edge onset has the highest Co edge onset and *vice versa*; a reciprocity between the cations seems to take place. The XANES in this data set is similar to previous XAS analyses of oxidation states in Co- and Ni-based oxides,[27] in which the intensity of the peak about 15 eV above the edge was correlated to the formal TM oxidation state: the white line was associated with unoccupied $3d^n$ states, and the higher energy peak with $3d^{n-1}$ or $3d^n + L_h$, where L_h signifies a ligand hole. Applying this hypothesis to our results, we see in both the Fe and Co K XAS a decrease in the $3d^{n-1}$ (TM^{4+}) and $3d^n$ (TM^{3+}) + L_h unoccupied states above the localized–delocalized carrier transition temperature. However, this result is puzzling as our previous measurements of the O K edge in BSCF powders quenched from medium and high temperatures showed a marked increase in the number of unoccupied O states just above the Fermi level for the samples with delocalized carriers.[28] Remaining changes in the XANES that

occur with heating represent the alteration of local cation coordination and lowering of symmetry with oxygen loss.[29]

From the Mössbauer and XAS data we can see that the initial iron oxidation state is in part 4+, but predominantly 3+. The room temperature magnetic components of samples with $x = 0.2$, $y = 0.2$ and $x = 0.5$, $y = 0.2$ reveal patterns typical of Fe^{3+} in octahedral sites; however, the reduced magnetic hyperfine fields of less than 50 T have to be connected to the presence of nearby oxygen vacancies. The other paramagnetic compositions $x = 0.5$, $y = 0.8$; $x = 0.8$, $y = 0.2$ exhibit Fe^{4+} and two species of equal spectral weight, attributed to dissociated trivalent iron with mixed oxidation states. Notably, these iron ions possess strongly distorted oxygen surroundings as expected from defects related to oxygen deficiency. That Fe and Co initially have oxidation states that are mostly 3+ is consistent with our previous findings from the soft XAS of BSCF powders quenched from 623 and 1173 K.[28] The presence of multiple Fe cation sites in BSCF at room temperature confirms the small polaron hopping mechanism for semiconductivity.

As BSCF is heated from the localized carrier regime (*ca.* 300–700 K) to the delocalized (*ca.* >700 K) the only change in the formal TM electronic state is the reduction of a small amount of TM^{4+} to TM^{3+}. The main charge carriers, electronic holes, which are created in the semiconducting region with increasing temperature are mainly of oxygen p character. This again shows the stability of the Fe^{3+} and Co^{3+} cations in the perovskite structure despite an environment of high temperature and high oxygen deficiency. The composition with $x = 0.2$, $y = 0.2$ is unique in that its transition temperature from localized to delocalized charge carriers is significantly higher (at 820 K) than the other compositions and it seems to revert to a semiconductor at about 1000 K (Fig. 1). As such, the XAS measurements for this sample were taken up to 1233 K, enabling the reduction of Co^{3+} to Co^{2+}, which could occur in tandem with the second electronic conductivity transition and phase change.

The lack of oxygen stoichiometry shown by the measurement of mostly TM^{3+} and imperfect octahedral coordination of the TM cations results in the strong oxygen exchange capability demonstrated by BSCF. That this material can undergo a ± 1% change in mass without any phase change shows its robustness towards temperature-induced oxygen loss and makes it promising for high temperature applications in which oxygen ion diffusion along with electronic conductivity is desired. However, in looking at the XAS results, it is clear that the initial state of both the iron and cobalt cations is not regained once the temperature cycle has been completed. Since the same thermal ramp rate was used for all three *in situ* techniques, this seeming anomaly cannot be due to inconsistent measurements. More likely is the case that while oxygen can be taken up by BSCF with cooling from high temperature at a rate of 8 K min^{-1}, it cannot be chemically incorporated into the compound to its full extent, and the transition metal cations are left in their high temperature, slightly reduced state. Over the course of one or two temperature cycles, our studies have shown that this does not seem to have an impact on the structural stability and total conductivity of BSCF, but with longer term cycling, the material performance could suffer when applied as a SOFC cathode.

Conclusions

For the first time, *in situ* high temperature X-ray absorption measurements at the Fe and Co K edges were performed on $Ba_{1-x}Sr_xCo_{1-y}Fe_yO_{3-\delta}$ powders, with $x = 0.5$, $y = 0.2$; $x = 0.5$, $y = 0.8$; $x = 0.2$, $y = 0.2$; and $x = 0.8$, $y = 0.2$. These results showed that Fe is predominantly 3+ from 300 to 1233 K, and Co is predominantly 3+ from 300 to 1073 K, but reduced to 2+ at higher temperatures. Room temperature Mössbauer spectroscopy detected three different atomic sites for Fe, again with a predominantly 3+ oxidation state. Two compositions are paramagnetic ($x = 0.5$, $y = 0.8$ and $x = 0.8$, $y = 0.2$) and the other two ($x = 0.2$, $y = 0.2$ and $x = 0.5$, $y = 0.2$) already have magnetic character at 300 K. X-Ray diffraction of BSCF was also done with *in situ* heating in air and showed that all the samples that are initially cubic perovskites remain so, while the one composition that started out with multiple phases (x, $y = 0.2$) transforms into the cubic phase with high temperature. The oxygen absorption and desorption of BSCF, creating a mass gain and loss of 1%, were measured with thermogravimetry. In view of engineering materials for SOFC cathodes, BSCF compositions rich in Sr and Co exhibit greater stability along with higher total conductivity.

Acknowledgements

The XAS and XRD measurements were performed on beamline BM01B (Swiss–Norwegian Beam Lines) of the European Synchrotron Radiation Facility (ESRF) in Grenoble, France, under experiment #01-01-735. We thank beamline scientists Hermann Emerrich and Wouter van Beek for their help.

References

1 Z. P. Shao and S. M. Haile, *Nature*, 2004, **431**, 170.
2 Z. H. Chen, R. Ran, W. Zhou, Z. P. Shao and S. M. Liu, *Electrochim. Acta*, 2007, **52**, 7343.
3 B. Wei, Z. Lu, X. Q. Huang, J. P. Miao, X. Q. Sha, X. S. Xin and W. H. Su, *J. Eur. Ceram. Soc.*, 2006, **26**, 2827.
4 P. Y. Zeng, Z. H. Chen, W. Zhou, H. Gu, Z. P. Shao and S. Liu, *J. Membr. Sci.*, 2007, **291**, 148.
5 S. McIntosh, J. F. Vente, W. G. Haije, D. H. A. Blank and H. J. M. Bouwmeester, *Chem. Mater.*, 2006, **18**, 2187.
6 S. McIntosh, J. F. Vente, W. G. Haije, D. H. A. Blank and H. J. M. Bouwmeester, *Solid State Ionics*, 2006, **177**, 1737.
7 S. Švarcová, K. Wiik, J. Tolchard, H. J. M. Bouwmeester and T. Grande, *Solid State Ionics*, 2008, **178**, 1787.
8 A. Yan, M. Cheng, Y. L. Dong, W. S. Yang, V. Maragou, S. Q. Song and P. Tsiakaras, *Appl. Catal., B*, 2006, **66**, 64; A. Yan, V. Maragou, A. Arico, M. Cheng and P. Tsiakaras, *Appl. Catal., B*, 2007, **76**, 320.
9 H. H. Wang, C. Tablet, A. Feldhoff and H. Caro, *J. Membr. Sci.*, 2005, **262**, 20.
10 J. Ovenstone, J.-I. Jung, J. S. Whilte, D. D. Edwards and S. T. Misture, *J. Solid State Chem.*, 2008, **181**, 576.
11 D. Beckel, A. Bieberle-Hutter, A. S. Harvey, A. Infortuna, U. P. Muecke, M. Prestat, J. L. M. Rupp and L. J. Gauckler, *J. Power Sources*, 2007, **173**, 325.
12 Z. Yang, A. S. Harvey, A. Infortuna and L. J. Gauckler, *J. Appl. Crystallogr.*, 2009, accepted.
13 M. Newville, *J. Synchrotron Radiat.*, 2001, **8**, 322.
14 J. F. Vente, S. McIntosh, W. G. Haije and H. J. M. Bouwmeester, *J. Solid State Electrochem.*, 2006, **10**, 581.

15 L.-W. Tai, M. M. Nasrallah, H. U. Anderson, D. M. Sparlin and S. R. Sehlin, *Solid State Ionics*, 1995, **76**, 259.
16 Q. S. Zhu, T. A. Jin and Y. Wang, *Solid State Ionics*, 2006, **177**, 1199.
17 L.-W. Tai, M. M. Nasrallah, H. U. Anderson, D. M. Sparlin and S. R. Sehlin, *Solid State Ionics*, 1995, **76**, 273.
18 C. S. Kim, Y. R. Uhm and J. C. Sur, *J. Korean Phys. Soc.*, 2000, **37**, 447.
19 S. Morimoto, K. Kuzushita and S. Nasu, *J. Magn. Magn. Mater.*, 2004, **272–276**, 127; M. Takano, J. Kawachi, N. Nakanishi and Y. Takeda, *J. Solid State Chem.*, 1981, **39**, 75; Y. R. Uhm, S. W. Lee, K.-T. Park, Y. Tomioka, Y. Tokura and C. S. Kim, *J. Appl. Phys.*, 2000, **87**, 4873.
20 Y. R. Uhm, K.-T. Park, C. S. Kim, Y. Tomioka and Y. Tokura, *J. Korean Phys. Soc.*, 2000, **37**, 430.
21 L. A. Isupova, Y. T. Pavlyukhin, V. A. Rogov, G. M. Alikina, S. V. Tsybulya, I. S. Yakovleva and V. A. Sadykov, *Mater. Res. Soc. Symp. Proc.*, 2005, **848**, FF10.5.
22 B. Buffat and M. H. Tuilier, *Solid State Commun.*, 1987, **64**, 401; J. E. Hahn, R. A. Scott, K. O. Hodgson, S. Doniach, S. R. Desjardins and E. I. Solomon, *Chem. Phys. Lett.*, 1982, **88**, 595; R. G. Schulman, Y. Yafet, P. Eisenberger and W. E. Blumberg, *Proc. Natl. Acad. Sci. U. S. A.*, 1976, **73**, 1384.
23 M. Wilke, G. M. Partzsch, R. Bernhardt and D. Lattard, *Chem. Geol.*, 2005, **220**, 143.
24 Y. Teraoka, M. Yoshimatsu, N. Yamazoe and T. Seiyama, *Chem. Lett.*, 1984, **13**, 893.
25 J.-W. Kim and S.-M. Park, *J. Electrochem. Soc.*, 2003, **150**, E560.
26 F. J. Berry, J. F. Marco and X. Ren, *J. Solid State Chem.*, 2005, **178**, 961; J. Herrero-Martin, G. Subias, J. Blasco, J. Garcia and M. C. Sanchez, *J. Phys.: Condens. Matter*, 2005, **17**, 4963.
27 J. E. Sunstrom, K. V. Ramanujachary, M. Greenblatt and M. Croft, *J. Solid State Chem.*, 1998, **139**, 388; A. Sahiner, M. Croft, Z. Zhang, M. Greenblatt, I. Perez, P. Metcalf, H. Jhans, G. Liang and Y. Jeon, *Phys. Rev. B: Condens. Matter*, 1996, **53**, 9745.
28 A. S. Harvey, Z. Yang, A. Infortuna, D. Beckel, J. A. Purton and L. J. Gauckler, *J. Phys.: Condens. Matter*, 2009, **21**, 015801, submitted.
29 R. Le Toquin, W. Paulus, A. Cousson, C. Prestipino and C. Lamberti, *J. Am. Chem. Soc.*, 2006, **128**, 13161.

